

## Manuscript Details

<b>Manuscript number</b>	ICARUS_2019_454_R1
<b>Title</b>	Constraining Ganymede's neutral and plasma environments through simulations of its ionosphere and Galileo observations
<b>Article type</b>	Research paper

### Abstract

Ganymede's neutral and plasma environments are poorly constrained by observations. Carnielli et al. (2019) developed the first 3D ionospheric model aimed at understanding the dynamics of the present ion species and at quantifying the presence of each component in the moon's magnetosphere. The model outputs were compared with Galileo measurements of the ion energy flux, ion bulk velocity and electron number density made during the G2 flyby. A good agreement was found in terms of ion energy distribution and bulk velocity, but not in terms of electron number density. In this work, we present some improvements to our model Carnielli et al. (2019) and quantitatively address the possible sources of the discrepancy found in the electron number density between the Galileo observations and our ionospheric model. We have improved the ion model by developing a collision scheme to simulate the charge-exchange interaction between the exosphere and the ionosphere. We have simulated the energetic component of the O<sub>2</sub> population, which is missing in the exospheric model of Leblanc et al. (2017) and added it to the original distribution, hence improving its description at high altitudes. These improvements are found to be insufficient to explain the discrepancy in the electron number density. We provide arguments that the input O<sub>2</sub> exosphere is underestimated and that the plasma production acts asymmetrically between the Jovian and anti-Jovian hemispheres. In particular, we estimate that the O<sub>2</sub> column density should be greater than  $10^{15} \text{ cm}^{-2}$ , i.e., higher than previously derived upper limits (and a factor 10 higher than the values from Leblanc et al. (2017)), and that the ionization frequency from electron impact must be higher in the anti-Jovian hemisphere for the G2 flyby conditions.

<b>Keywords</b>	Ganymede; Ionospheres; Jupiter; Satellites; Satellite Atmospheres
<b>Corresponding Author</b>	Gianluca Carnielli
<b>Corresponding Author's Institution</b>	Imperial College London
<b>Order of Authors</b>	Gianluca Carnielli, Marina Galand, Ronan MODOLO, Francois Leblanc, Arnaud Beth, Xianzhe jia
<b>Suggested reviewers</b>	Andrew Poppe, Benjamin Teolis, Christina Plainaki, Carol Paty, robert johnson

## Submission Files Included in this PDF

### File Name [File Type]

refereeAnswers.docx [Response to Reviewers]

Highlights.docx [Highlights]

manuscript.pdf [Manuscript File]

To view all the submission files, including those not included in the PDF, click on the manuscript title on your EVISE Homepage, then click 'Download zip file'.

# Answers to referee's comments on the manuscript: Constraining Ganymede's neutral and plasma environments through simulations of its ionosphere and Galileo observations

G. Carnielli, M. Galand, F. Leblanc, R. Modolo, A. Beth, X. Jia

## Preamble:

We would like to warmly thank both referees for their constructive comments, suggestions, and time devoted to review the manuscript. By considering all the comments received, we have updated our work. In blue are the original referee's comments, in red are our answers.

## Reviewer 1:

This paper sheds new light on the Ganymede gas and plasma environment and the results will be useful for the proposed missions to the Jovian system. It builds on previous papers, the most recent has now appeared in Icarus.

This new work, as the authors say, is not a unique solution since the data they compare to is limited, but the results are suggestive. The work indicates that simply adding a hot O<sub>2</sub> component to their previous modeling was not sufficient to explain the dearth in their model electron densities, though how hot O<sub>2</sub> might help was not made clear. But they showed that increasing the estimates of the atmospheric O<sub>2</sub> column density and the electron ionization frequency would allow them to understand and model the available data.

This is all useful so that the work should be published. But was there a reason one thought the hot O<sub>2</sub> might be important? It would seem to have, a priori, a small effect. Also having to wade through what is not useful (hot O<sub>2</sub>) to get to the point that one might need to boost the crude estimate of O<sub>2</sub> density and the electron impact ionization frequency seemed an effort.

Energetic neutrals are produced in a region where the electron density was found to be underestimated, hence it seems reasonable to verify quantitatively their impact on the plasma density through simulations and to report it. In addition, the results obtained from the study of hot O<sub>2</sub> are relevant for the upcoming JUICE mission. In this context, measurements can be compared to our simulations, and they can be used as a validation tool for our model.

As correctly pointed out by the reviewer, hot O<sub>2</sub> turns out to be irrelevant for explaining the discrepancy between the ionospheric model and the PWS observations. As such, we moved the discussion of energetic neutrals (Section 2.2) to the appendix, achieving also a considerable reduction in the length of the main body of the manuscript.

A small paragraph was added to substitute Section 2.2 (lines 294-303):

“We used the collision scheme to simulate, through ad hoc simulations, the dynamics of energetic neutrals produced through charge-exchange with the ionosphere. As a result, we derived the first 3D maps for hot O<sub>2</sub>, which was not included in the exospheric model of Leblanc (2017). The results of these simulations are presented in Appendix A. As it turns out, the inclusion of energetic neutrals at high altitudes does not address the issue of underestimated plasma density along the Galileo trajectory. Nonetheless, the results from this study are relevant for comparing with future in situ measurements by the Particle Environment Package (PEP) on board the JUICE spacecraft.”

The work should be published, but the manuscript seems much longer than necessary to make their points. I started noting some awkward statements (even one of the first sentences: lines 30- 31 ---are Ganymede’s ionospheric ions causing sputtering and the ‘latter’ is assessed?). Even later in lines 425 - 433 a single sentence would seem to do.

Line 30-31 [now lines 41-43] has been changed to: “...sputtering from Jovian magnetospheric ions and from Ganymede's ionospheric ions (the ionospheric contribution has been assessed for the first time in Carnielli et al., submitted)”.

In regard to the content in lines 425-433 [now lines 347-355], we find it all to be useful for the reader, and that it cannot be merged into a single sentence. Hence, we left it as it is.

Therefore, I strongly support publishing this after the authors make an effort to simplify and shorten the writing. For instance, since their calculations are related to those in their previous papers they could rely more on those papers. If hot O<sub>2</sub> is not important they could address that more efficiently and get to the point of what is important sooner.

See our response to the first point.

Again, the work is good and should be published. This referee does not need to see it again.

## Reviewer 2

This manuscript represents a very valuable contribution to an improved understanding of Ganymede's exosphere and plasma environment. It provides an independent constraint on the exospheric density, which is presently poorly constrained. It makes good sense that an improved understanding of the electron density would provide a better constraint on the exospheric density implied by the observations, it was explicitly mentioned by Hall et al. that a future improved understanding of the electron density would allow a much more accurate determination of the exospheric density. I have no major issues with the paper, and recommend it be published largely as is, after the authors take into consideration the one point below.

The authors cite the Carlson et al. 1973 "detection" of Ganymede's exosphere. However, I am not aware of anyone who thinks that Ganymede actually has an exosphere with pressure of a microbar, including Carlson. This paper has been largely discounted over time. The observations are poor, they are made in the visible, no plausible exosphere was discussed or modeled based on these observations, the only suggestion for a possible atmospheric constituent was nitrogen. These same types of observations were used by the same authors to rule out an exosphere on Io, which we now know well has a much more robust atmosphere than that of Ganymede. This claimed detection by Carlson et al. was superseded by the Broadfoot et al. 1979 non-detection and upper limit, which was much more stringent and based on much higher quality data. I would urge the authors to give a more complete history of the detections and non-detections, i.e., I suggest that you also cite the Broadfoot paper and its upper limit, which is inconsistent with the Carlson "detection." I would also recommend that you compare your new constraint on the exospheric density/pressure with these two historical constraints, in addition to comparing it with the Hall et al. results.

We have modified the introduction as follows (lines 27-39):

“Quantitative observations of Ganymede's exosphere started with Carlson et al. (1973) who exploited a stellar occultation by Ganymede to observe the red and blue regions of the visible spectrum. These observations effectively marked the discovery of a thin gas envelope around the moon, indicating the presence of an atmosphere with a surface pressure greater than about  $10^{-3}$  millibar.

With the arrival of Voyager 1 at Jupiter in 1979, the onboard UVS spectrometer took advantage of an occultation of K Centauri by Ganymede to make limb observations in the UV spectrum range. These new measurements placed an upper limit of  $2 \times 10^{-8}$  millibar - or equivalently  $1.5 \times 10^9 \text{ cm}^{-3}$  - for the surface density of suspected dominant species like  $\text{H}_2\text{O}$  and  $\text{O}_2$  (Broadfoot et al., 1981), which is a factor of  $10^{-5}$  lower than the lower limit derived by Carlson et al. (1973) and which appears to be unrealistically high.”

As for comparing our constraint on the exospheric density with Broadfoot et al. (1981), we have added a few sentences in the conclusions, in the same paragraph where we compare with previous estimates by Hall et al. and exospheric models (lines 550 - 555):

“The comparison with Broadfoot et al. (1981) is limited since they only provided an upper limit for the exospheric surface density  $1.5 \times 10^9 \text{ cm}^{-3}$ , and not for the column density. Considering only this value and assuming the same scale height as in the model of Leblanc et al. (2017), the required exospheric configuration is within the limit derived by Broadfoot et al. (1981).”

I'd also suggest that in future the authors consider using their modeling to predict the auroral emission morphology, and then compare this with the auroral observations, which provide another excellent constraint on the modeling. This is outside the scope of the present paper but would be a valuable additional test of the models.

Thank you for the suggestion. We plan to address this in a future study.

## Highlights

- Ganymede O<sub>2</sub> exosphere should be denser than previously anticipated. While previous observation-driven and model-based estimates found a column density of the order of 10<sup>14</sup> cm<sup>2</sup>, we find that this value should exceed 10<sup>15</sup> cm<sup>2</sup>.
- We have improved the ionospheric model of Carnielli et al. (2019) by adding collisions between ion and neutral species, and found that this process has an appreciable effect on the ion distribution only at altitudes below 200 km.
- Through test particle simulations, we generated the first 3D maps of density and velocity of energetic O<sub>2</sub> in Ganymede's exosphere, a population that will be assessed by the JUICE-PEP instrument. In this context, these 3D maps will be useful for interpreting in situ data.

# Constraining Ganymede’s neutral and plasma environments through simulations of its ionosphere and Galileo observations

G. Carnielli<sup>a,\*</sup>, M. Galand<sup>a</sup>, F. Leblanc<sup>b</sup>, R. Modolo<sup>c</sup>, A. Beth<sup>a</sup>, X. Jia<sup>d</sup>

<sup>a</sup>*Department of Physics, Imperial College London, SW7 2AZ, London, United Kingdom*

<sup>b</sup>*LATMOS/IPSL, CNRS, Sorbonne Université, UVSQ, Paris, France*

<sup>c</sup>*LATMOS/IPSL, UVSQ Université Paris-Saclay, UPMC Univ. Paris 06, Guyancourt, France*

<sup>d</sup>*Department of Climate and Space Sciences and Engineering, University of Michigan, Ann Arbor, MI 48109-2143, USA*

---

## Abstract

1 Ganymede’s neutral and plasma environments are poorly constrained by  
2 observations. Carnielli et al. (2019) developed the first 3D ionospheric model  
3 aimed at understanding the dynamics of the present ion species and at quan-  
4 tifying the presence of each component in the moon’s magnetosphere. The  
5 model outputs were compared with Galileo measurements of the ion energy  
6 flux, ion bulk velocity and electron number density made during the G2 flyby.  
7 A good agreement was found in terms of ion energy distribution and bulk  
8 velocity, but not in terms of electron number density.

9 In this work, we present some improvements to our model (Carnielli et al.,  
10 2019) and quantitatively address the possible sources of discrepancy found  
11 in the electron number density between the Galileo observations and our  
12 ionospheric model. We have improved the ion model by developing a collision  
13 scheme to simulate the charge-exchange interaction between the exosphere  
14 and the ionosphere. We have simulated the energetic component of the O<sub>2</sub>

---

\*Principal corresponding author:  
*Preprint submitted to Icarus*  
Email address: gianluca.carnielli10@imperial.ac.uk (G. Carnielli) January 11, 2020

15 population, which is missing in the exospheric model of Leblanc et al. (2017)  
16 and added it to the original distribution, hence improving its description at  
17 high altitudes. These improvements are found to be insufficient to explain  
18 the discrepancy in the electron number density. We provide arguments that  
19 the input O<sub>2</sub> exosphere is underestimated and that the plasma production  
20 acts asymmetrically between the Jovian and anti-Jovian hemispheres. In  
21 particular, we estimate that the O<sub>2</sub> column density should be greater than  
22 10<sup>15</sup> cm<sup>-2</sup>, i.e., higher than previously derived upper limits (and a factor 10  
23 higher than the values from Leblanc et al. (2017)), and that the ionization  
24 frequency from electron impact must be higher in the anti-Jovian hemisphere  
25 for the G2 flyby conditions.

*Keywords:* Ganymede, Ionospheres, Jupiter, satellites, Satellite,  
atmospheres

---

## 26 **1. Introduction**

27 Quantitative observations of Ganymede’s exosphere started with Carlson  
28 et al. (1973), who exploited a stellar occultation by Ganymede to observe the  
29 red and blue regions of the visible spectrum. These observations effectively  
30 marked the discovery of a thin gas envelope around the moon, indicating  
31 the presence of an atmosphere with a surface pressure greater than about  
32 10<sup>-3</sup> millibar.

33 With the arrival of Voyager 1 at Jupiter in 1979, the onboard UVS spec-  
34 trometer took advantage of an occultation of K Centauri by Ganymede to  
35 make limb observations in the UV spectrum range. These new measurements  
36 placed an upper limit of 2×10<sup>-8</sup> millibar – or equivalently 1.5×10<sup>9</sup> cm<sup>-3</sup> – for



37 the surface density of suspected dominant species like H<sub>2</sub>O and O<sub>2</sub> (Broad-  
38 foot et al., 1981), which is inconsistent with Carlson et al. (1973) being a  
39 factor of 10<sup>-5</sup> lower than their derived lower limit.

40 The major exospheric sources are sublimation of the icy surface in the sub-  
41 solar region, sputtering from Jovian magnetospheric ions and from Ganymede's  
42 ionospheric ions (the ionospheric contribution has been assessed for the first  
43 time in Carnielli et al., submitted). Despite the confirmation of the presence  
44 of an exosphere by remote-sensing observations, little is known with certainty  
45 regarding its properties. The presence of O and O<sub>2</sub> has been inferred from  
46 UV emissions at 1304 Å and 1356 Å measured remotely by the Hubble Space  
47 Telescope (Hall et al. (1998); Feldman et al. (2000); McGrath et al. (2013);  
48 Molyneux et al. (2018)). The 3D distribution of these species around the  
49 moon is poorly constrained, and our current knowledge builds primarily on  
50 exospheric models that have been developed in the past 12 years (e.g., Mar-  
51 conic (2007); Turc et al. (2014); Plainaki et al. (2015); Shematovich (2016);  
52 Leblanc et al. (2017)). These models made assumptions regarding the sput-  
53 tering and sublimation fluxes, and validated their outcome by comparing the  
54 column density of O<sub>2</sub> with that derived by Hall et al. (1998) from OI FUV  
55 emissions.

56 Hall et al. (1998) estimated an O<sub>2</sub> column density in the range 10<sup>14</sup> –  
57 10<sup>15</sup> cm<sup>-2</sup>. Exospheric models found that O<sub>2</sub> dominates in the region of  
58 open magnetic field lines (or everywhere, in the case of the model of Leblanc  
59 et al. (2017), in the case of a low ice sublimation rate in the subsolar region).  
60 We argue that the estimate of Hall et al. (1998) was made on the basis of  
61 strong assumptions regarding the electron distribution. Hall et al. (1998)

62 derived the O<sub>2</sub> column density from the observed UV emissions assuming a  
63 hypothetical distribution of electrons. They made use of the electron number  
64 density recorded during the Galileo G1 and G2 flybys, those which occurred  
65 closest to the moon and contained primarily electrons from Ganymede’s iono-  
66 sphere rather than the Jovian magnetosphere (Carnielli et al., 2019). Their  
67 estimate assumed that all electrons ( $\sim 100 \text{ cm}^{-3}$  at the surface) are able to  
68 excite auroral emissions on O<sub>2</sub>, i.e., that all electrons are energetic enough  
69 to do so. The dissociative excitation of O<sub>2</sub> has an energy threshold around  
70 14–15 eV and the associated cross-section peaks near 100 eV (Kanik et al.,  
71 2003). Hence, ionospheric electrons, which dominate inside the magneto-  
72 sphere (Carnielli et al., 2019), would need to undergo significant accelera-  
73 tion, and the way this would occur is not clear, as argued also by Eviatar  
74 et al. (2001a). However, a recent modeling study by Zhou et al. (2019)  
75 suggests that energization through magnetic reconnection at the upstream  
76 magnetopause can contribute as much as 40% of the energy flux required  
77 to produce the observed auroral emissions. Hall et al. (1998) rightly had to  
78 make assumptions regarding the electron distribution in the absence of in situ  
79 measurements near the separatrix region, i.e., where the emissions dominate.  
80 However, the closest approach for G1 and G2 occurred inside the northern  
81 Alfvén wing, where the electron distribution is likely to differ significantly  
82 from that near the boundary between open and closed magnetic field lines.  
83 As a consequence, the distribution used by Hall et al. (1998) might not be  
84 the suitable one in order to retrieve the O<sub>2</sub> column density from the OI FUV  
85 emissions. A way to reproduce the observations in a more realistic way would  
86 be to reduce the density of exciting electrons, which implies to increase that

87 of O<sub>2</sub>. In this work, we present independent arguments to show that, in fact,  
88 the O<sub>2</sub> exosphere should be denser than what was previously estimated and  
89 modeled.

90 Ganymede’s ionosphere is also poorly constrained in terms of observa-  
91 tions, which come only from the Galileo mission. Using radio occultation  
92 measurements, Kliore (1998) derived an upper limit of 4000 cm<sup>-3</sup> for the  
93 electron number density at the surface. Along the G1 and G2 flybys, the  
94 PWS instrument on board Galileo measured the electron number density  
95 (primarily of ionospheric origin near closest approach), while the PLS in-  
96 strument recorded the ion bulk flow velocities and ion energy spectra (Frank  
97 et al., 1997). For the G2 flyby, the flow was originally interpreted by Barth  
98 et al. (1997) as escaping hydrogen ions. However, this was later reinterpreted  
99 as a flow of oxygen ions by Vasyliūnas and Eviatar (2000), which is supported  
100 by the MHD simulation results of Jia et al. (2009), and a combination of both  
101 species by Paty et al. (2008), who argued, using the outcome from their MHD  
102 simulations, that only H<sup>+</sup> would be detected by the PLS instrument. More  
103 recently, Collinson et al. (2018) re-analyzed the PLS data from the G1 and  
104 G2 flybys, showing different fits for different assumed ion masses. Remark-  
105 ably, for the G2 flyby none of the fits can match the electron density profile  
106 – which, assuming quasi-neutrality, should equal to the total ion density –  
107 derived from PWS and reported in Eviatar et al. (2001b). In summary, the  
108 ionospheric composition is a subject of debate.

109 Simplistic efforts to characterize the ionosphere have been made by Evi-  
110 atar et al. (2001b) and Cessateur et al. (2012). More recently, we have  
111 developed the first 3D multi-species test particle model of Ganymede’s iono-

112 sphere (Carnielli et al., 2019). In this model, ions are generated from the  
113 ionization of the neutral exosphere, whose 3D configuration is taken from  
114 the recent model of Leblanc et al. (2017); they move in the electromagnetic  
115 field environment modeled by Leclercq et al. (2016) or Jia et al. (2009), and  
116 the distribution moments (number density, bulk velocity, temperature) are  
117 collected on a 3D spherical grid. Both the model of Eviatar et al. (2001b)  
118 and Carnielli et al. (2019) found the ionosphere to be dominated by  $O_2^+$   
119 near the surface, including the location of closest approach of the Galileo  
120 spacecraft during G2. This is supported by our finding that the major ion  
121 species observed by PLS was  $O_2^+$  (Carnielli et al., 2019). A good agreement  
122 of our modeled output was found with the Galileo data in terms of ion energy  
123 distribution. A discrepancy, however, was found in terms of electron number  
124 density, with an underestimation of the modeled density compared to the  
125 measured one by more than one order of magnitude. Considering that the  
126 energy distribution agrees well with observations, which suggests that the  
127 fields describe well the field configuration at the time of the G2 flyby, it was  
128 concluded that the input exosphere is the likely cause for the discrepancy.

129 In this work, we have made improvements to the ionospheric model and  
130 quantitatively addressed the possible sources of discrepancy between our  
131 model and observations in terms of electron number density. Our origi-  
132 nal ionospheric model, presented in Carnielli et al. (2019), did not include  
133 collisions between ions and neutrals. Collisions with the neutral exosphere  
134 lead to a transfer of kinetic energy from the ionosphere to the exosphere,  
135 resulting in an increased ion density closed to the surface. In addition, the  
136 input exosphere from the model of Leblanc et al. (2017) did not include the

137 energetic  $O_2$  component, whose source is charge-exchange with ionospheric  
138 ions; but which ultimately is also a source of ionospheric ions. To address  
139 these limitations, we have developed a collision scheme to simulate the in-  
140 teraction between the major ions and neutral species in the atmosphere, i.e.,  
141  $O_2^+$ ,  $O^+$  and  $O_2$ . From this scheme, we have derived a production map for  
142 energetic  $O$  and  $O_2$  and simulated the dynamics of these populations with  
143 ad hoc simulations. As it turns out, these changes do not improve the com-  
144 parison of the electron number density along the G2 flyby. Hence, we have  
145 investigated further the discrepancy by searching for an appropriate physical  
146 configuration, in terms of exospheric densities and ionization sources, with  
147 which the simulation results are consistent with the Galileo observations.

148 The paper is organized as follows. Section 2 describes the collision scheme  
149 and its effect on the outputs of the ionospheric model. In Section 3 we  
150 describe an unsuccessful attempt to fit the Galileo observations by adapting  
151 only the new configuration of the neutral exosphere, while in Section 4 we  
152 describe a successful attempt by adapting both the new configuration of the  
153 neutral exosphere and the ionization sources. Finally, Section 5 summarizes  
154 and discusses the results achieved in this study.

## 155 **2. Improvements to the ionospheric model**

### 156 *2.1. Modeling ion-neutral interactions*

#### 157 *2.1.1. Motivation*

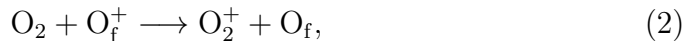
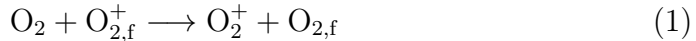
158 Carnielli et al. (2019) showed that ionospheric particles interact more fre-  
159 quently with the neutral exosphere close to the surface (below approximately  
160 200 km), where the timescale of collisions between ionospheric particles and

161 neutral species is comparable to that of transport (cf. Figure 6 and Sec-  
162 tion 3.4.2 in Carnielli et al., 2019). However, they did not include collisions  
163 as they estimated that the ion production rate from charge-exchange is negli-  
164 gible compared to those from photo- and electron-impact ionization. In fact,  
165 the collision process, by slowing down the ion, could have an effect on the  
166 ionospheric configuration to the extent that it leads to an increased amount  
167 of time spent inside the cell, leading to an increased ion number density.  
168 Despite providing a measure of how important collisions can be in terms of  
169 production rate, the study presented in Carnielli et al. (2019) could not  
170 determine the effects that collisions would have on the dynamical evolution  
171 of the test-particle trajectories and on the distribution moments maps. In  
172 addition, in a denser exosphere (as later discussed in Section 3) collisions  
173 become even more important to consider. Regardless of the exospheric con-  
174 figuration, including collisions leads to a more realistic simulation, thus we  
175 have developed a collision scheme that has been integrated into the original  
176 model described in Carnielli et al. (2019).

### 177 2.1.2. *Collision scheme*

The interaction between ionized and neutral species involves momentum transfer collisions and charge-exchange reactions. Since in the exosphere modeled by Leblanc et al. (2017)  $O_2$  is the dominant component (close to the surface where densities are highest and collisions matter), we have considered only this neutral species in the collision scheme. Banks (1966) showed that at energies above 0.5 eV, which applies to Ganymede’s ionosphere, the neutral and ion species undergo charge-exchange rather than momentum transfer collisions. Due to the dominance of  $O_2^+$  and  $O^+$  in the ionosphere (Carnielli

et al., 2019), combined with their higher cross-section for charge-exchange with O<sub>2</sub>, we have considered only these two ion species in the collision scheme. More specifically, the following reactions have been considered:



178 where ‘f’ means fast. Charge-exchange between O<sub>2</sub> and O<sup>+</sup> has been con-  
 179 sidered also with Jovian O<sup>+</sup> ions, which constitute the majority of the bulk  
 180 plasma sheet population (Neubauer, 1998) (see Section 5.1.1 in Carnielli et  
 181 al. (2019) for a description of how Jovian ions were simulated).

182 Ions undergo charge-exchange with the neutral exosphere at all times at  
 183 a given rate,  $\nu_{i,n}^{cx}$ , given by:

$$\nu_{i,n}^{cx} = n_n \sigma_{i,n}^{cx}(E) |\vec{v}_i - \vec{v}_n|, \quad (3)$$

184 where  $\sigma_{i,n}^{cx}$  is the energy-dependent charge-exchange cross-section between  
 185 neutral species  $n$  and ion species  $i$ ,  $\vec{v}_n$  and  $\vec{v}_i$  their velocity, and  $n_n$  the local  
 186 number density of  $n$ . The values for the energy-dependent cross-section with  
 187 O<sub>2</sub> were taken from Stebbings et al. (1963) for O<sub>2</sub><sup>+</sup> and from Lindsay and  
 188 Stebbings (2005) for O<sup>+</sup>. The energy  $E$  refers to the relative kinetic energy  
 189 between  $i$  and  $n$ . In the simulations,  $i$  always moves significantly faster  
 190 compared to  $n$ , thus  $E$  refers simply to the kinetic energy of  $i$  and  $\vec{v}_n$  is  
 191 neglected, i.e.,  $n$  is assumed to be stationary in the charge-exchange process.

192 Mathematically, the probability of charge-exchange (CX) occurring be-  
 193 tween time  $t$  and  $t + \Delta t$ , which is an indication of the fraction of test particle  
 194 (hereafter referred to as ‘MP’) that exchanges an electron with the neutral

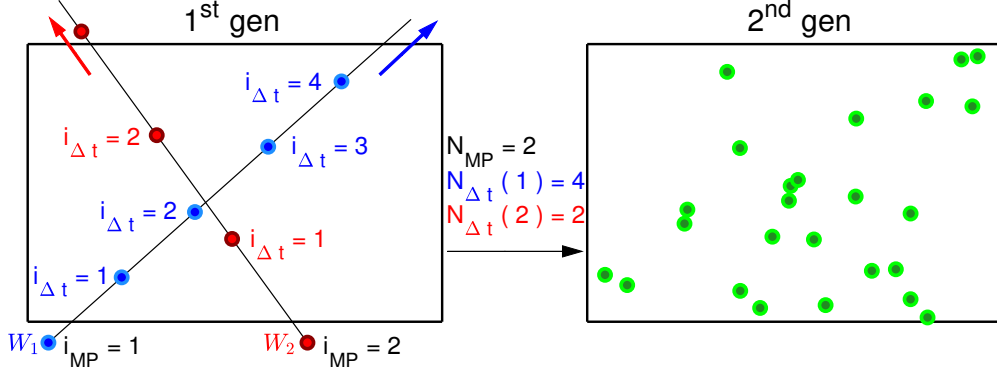


Figure 1: Schematic diagram of the collision scheme. See text for a full explanation.

195 population, can be formulated by the following expression (Modolo et al.,  
 196 2016):

$$p_{i,n}^{CX}(t \rightarrow t + \Delta t) = 1 - \exp^{-\nu_{i,n}^{cx} \Delta t}. \quad (4)$$

197 The probability tends to be 0 for a very short time interval and increases in  
 198 time proportionally to the reaction frequency  $\nu_{i,n}^{cx}$ , defined in Equation 3.

199 Figure 1 shows a schematic diagram of the collision scheme. In the simu-  
 200 lations, test particles are generated from ionization of the neutral exosphere,  
 201 or belong to the plasma sheet in the case of Jovian  $O^+$  ions. We refer to these  
 202 test particles as belonging to the 1<sup>st</sup> generation. These correspond to those  
 203 simulated also in the collisionless scenario. The left panel in Figure 1 shows  
 204 a simplified exospheric grid cell (the rectangle) crossed by two test-particle  
 205 trajectories belonging to the 1<sup>st</sup> generation. The trajectories look straight in  
 206 order to simplify the visualization, but in the simulation they are determined  
 207 by the local electromagnetic field. Each test particle has an index ‘ $i_{MP}$ ’ and  
 208 a weight  $W_{i_{MP}}$ , indicating the number of physical particles represented.

209 At each timestep  $i_{\Delta t}$ , the test particle interacts with the local neutral



210 environment, and its weight is reduced by an amount equal to the fraction  
 211  $p_{i_{\Delta t}, i_{MP}}^{CX}$  of MP that undergoes charge-exchange. This approach has been  
 212 implemented previously by Modolo et al. (2016) and validated by Chanteur  
 213 et al. (2009) and Koutroumpa et al. (2012). As the particle's weight is re-  
 214 duced at each timestep  $k$  by  $(1 - p_k^{CX}, i_{MP})$ , its weight loss at  $i_{\Delta t} \geq 2$  is:

$$W_{lost}(i_{\Delta t}) = W_{i_{MP}} p_{i_{\Delta t}, i_{MP}}^{CX} \prod_{k=1}^{i_{\Delta t}-1} (1 - p_{k, i_{MP}}^{CX}). \quad (5)$$

215 The lost weight is deposited and accumulated in the exospheric grid cell.  
 216 In the left panel of Figure 1, the red particle ( $i_{MP} = 2$ ) deposits part of  
 217 its weight at steps  $i_{\Delta t} = 1$  and  $i_{\Delta t} = 2$  (only when it is found inside the  
 218 exospheric grid cell). Instead, the blue particle ( $i_{MP} = 1$ ) deposits part of its  
 219 weight at four iterations. At the first iteration inside the cell, i.e.,  $i_{\Delta t} = 1$ ,  
 220 the red particle deposits a weight equal to  $p_{1,2}^{CX} W_2$ . The first sub-index refers  
 221 to the iteration inside the cell, and the second index corresponds to the value  
 222 of  $i_{MP}$ . After the first iteration, the MP's weight is reduced to  $(1 - p_{1,2}^{CX}) W_2$ .  
 223 At  $i_{\Delta t} = 2$  the particle deposits a weight equal to  $p_{2,2}^{CX} (1 - p_{1,2}^{CX}) W_2$ , and so  
 224 on. The same applies to the blue particle, which reduces its weight at the  
 225 four iterations during which it is found inside the exospheric cell. The total  
 226 weight deposited can be expressed as follows:

$$W = \sum_{i_{MP}=1}^{N_{MP}} W_{i_{MP}} \left( p_{1, i_{MP}}^{CX} + \sum_{i_{\Delta t}=2}^{N_{\Delta t}(i_{MP})} p_{i_{\Delta t}, i_{MP}}^{CX} \prod_{k=1}^{i_{\Delta t}-1} (1 - p_{k, i_{MP}}^{CX}) \right), \quad (6)$$

227 where  $N_{MP}$  is the number of test particles of the 1<sup>st</sup> generation that cross  
 228 the exospheric cell and  $N_{\Delta t}(i_{MP})$  is the number of iterations spent by test  
 229 particle  $i_{MP}$  inside the cell. The lost weight is then reassigned to a newly-  
 230 born test particle, belonging to the 2<sup>nd</sup> generation, which represents those

231 stationary ions produced from charge-exchange. These are initialized with  
232 a null velocity (because neutrals are assumed at rest) and a weight deter-  
233 mined by the accumulated charge-exchange in the cell. To have sufficient  
234 statistics, typically 50 of such MPs are produced in each cell at random po-  
235 sitions. These MPs – shown as green in the right panel of Figure 1 – can  
236 undergo further charge-exchange or, for the last generation considered, can  
237 be assumed to be collisionless. The user defines the number of generations  
238 to be simulated. In theory, charge-exchange should be calculated with each  
239 generation of MPs, which would make the simulation indefinitely long. In  
240 practice, MPs in higher generations carry only a fraction of the weight com-  
241 pared to the parent MPs, therefore calculating the charge-exchange process  
242 for new generations becomes progressively irrelevant. We have verified that  
243 including five generations is enough for the convergence of the results.

## 244 *2.2. Effects of collisions*

245 The physical effect of charge-exchange in the ionospheric model is to slow  
246 down test particles. If it takes more effort for the test particle of a species  
247 compared to another to be accelerated again by the fields after the collision,  
248 then we expect the effect of collisions to be more visible for this species. Due  
249 to the higher inertial mass of  $\text{O}_2^+$  compared to  $\text{O}^+$ , the effects of collisions  
250 were seen to be more important for the former species. Thus, here only the  
251 effects of collisions for  $\text{O}_2^+$  are discussed.

252 Figure 2 shows the average – over latitude and longitude –  $\text{O}_2^+$  number  
253 density obtained from simulations with and without collisions (red and blue  
254 curves, respectively). For the simulation with collisions, the green curve  
255 shows the contribution from the first generation, and the orange curve that

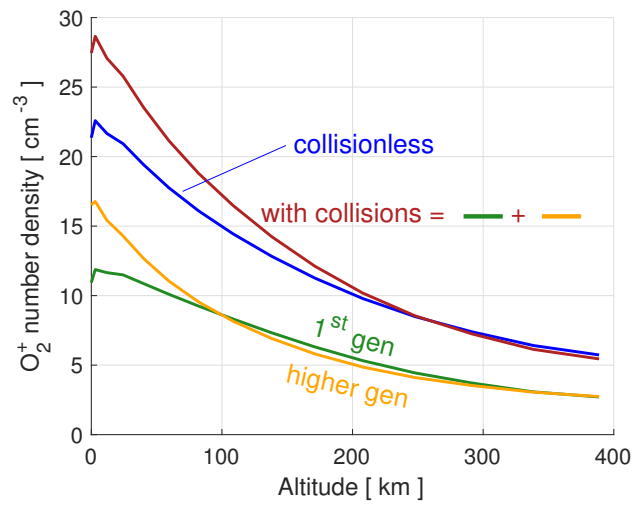


Figure 2: Average (over latitude and longitude)  $O_2^+$  number density as a function of altitude. Blue curve: Simulation without collisions. Red curve: Simulation with collisions. Green curve: Contribution from the first generation of test particles. Orange curve: Contribution from higher generations. The sum of the green and orange curves corresponds to the red curve.

256 from higher generations (in total, 5 generations were simulated): the sum of  
257 these two contributions represents the total contribution (red curve). Overall,  
258 the effect of collisions is to boost the  $\text{O}_2^+$  number density close to the surface,  
259 where the charge-exchange frequency is highest. The energetic  $\text{O}_2$  population  
260 provides a negligible contribution to the charge-exchange due to the low  
261 number density compared to the thermal population close to the surface.  
262 This applies also to the number density profile of energetic  $\text{O}_2$  from Marconi  
263 (2007), which is 3 orders of magnitude higher compared to that found by  
264 our simulations. Below approximately 260 km ( $\approx 0.1 R_G$ ), collisions lead to  
265 an increased number density (up to 30% near the surface), while at higher  
266 altitudes they result in a slight decrease. Although Figure 2 shows the average  
267 value over all latitudes and longitudes, this trend is seen everywhere around  
268 Ganymede, including the Alfvén wings and the equatorial region (not shown).

269 The density increase below 260 km is associated with the larger time  
270 spent in this region by test particles from higher generations, i.e., those  
271 which underwent charge-exchange with  $\text{O}_2$ : close to the surface, the particles  
272 from higher generations (orange curve) dominate in terms of number density  
273 compared with those from the first generation (green curve). Physically, this  
274 means that upon collision, test particles tend to stay near the surface and  
275 eventually impact instead of escaping, like those which did not undergo any  
276 collision. In contrast, at altitudes above 260 km the simulation with collisions  
277 yields a slightly lower density compared to the collisionless simulation. Such  
278 a migration towards the surface can be explained in terms of the electric field  
279 from the MHD model, whose radial component, on average, points towards  
280 the surface (not shown) at altitudes below 260 km. In other words, due to

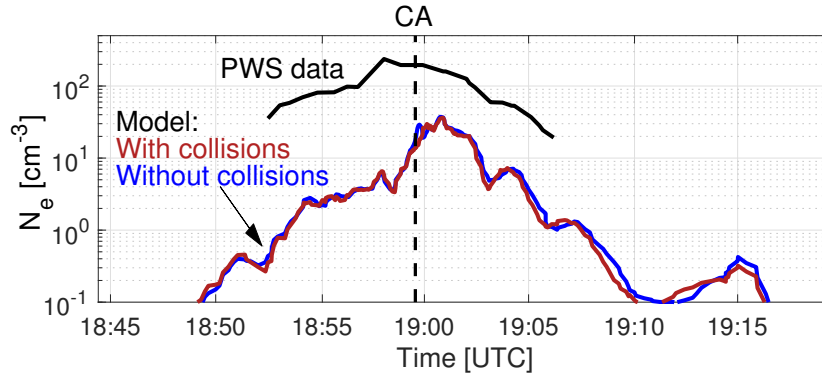


Figure 3: Electron number density along the G2 flyby as measured by: PWS (black), a simulation without collisions (blue) and one with collisions (red).

281 energy conservation MPs that are created with null velocity from charge-  
 282 exchange accelerate to a region of lower electric potential, i.e., closer to the  
 283 surface, compared to their parent MP which is at the same physical position  
 284 but has higher kinetic energy.

285 Figure 2 indicates that at 260 km, which corresponds to the distance  
 286 of closest approach of the Galileo spacecraft during the G2 flyby, charge-  
 287 exchange has almost no effect on the number density of  $O_2^+$ , at least on  
 288 average. This is demonstrated by Figure 3, which shows the electron number  
 289 density along the G2 flyby for the two simulations (blue curve for the one  
 290 without collisions and red curve for the one with collisions). The red and  
 291 blue curves almost overlap each other, confirming that collisions have no  
 292 appreciable effect over this altitude range. For reference, the electron density  
 293 measured by the PWS instrument is plotted in black.

294 We used the collision scheme to simulate, through ad hoc simulations,  
 295 the dynamics of energetic neutrals produced through charge-exchange with

296 the ionosphere. As a result, we derived the first 3D maps for hot O<sub>2</sub>, which  
297 was not included in the exospheric model of Leblanc et al. (2017). The  
298 results of these simulations are presented in Appendix A. As it turns out,  
299 the inclusion of energetic neutrals at high altitudes does not address the issue  
300 of underestimated plasma density along the Galileo trajectory. Nonetheless,  
301 the results from this study are relevant for comparing with future in situ  
302 measurements by the Particle Environment Package (PEP) on board the  
303 JUICE spacecraft.”

304 In summary, we conclude that including the energetic component of the  
305 O<sub>2</sub> population, therefore increasing its density at high altitudes, and in-  
306 cluding collisions in the ionospheric model are not sufficient to explain the  
307 discrepancy in number density between the model and observations.

### 308 **3. Optimizing Ganymede’s exosphere in light of Galileo observa-** 309 **tions**

310 Considering that the input electric and magnetic fields from the MHD  
311 model of Jia et al. (2009) provide a good description of the ion dynamics  
312 and lead to a good agreement with the observed ion energy spectrogram  
313 along the G2 flyby (Carnielli et al., 2019), and that collisions are insufficient  
314 to explain the order of magnitude gap between the modeled and observed  
315 electron number density, we have identified the neutral exosphere as a source  
316 of discrepancy.

317 In exospheric models, the ejection rate of neutral gases from Ganymede’s  
318 icy surface has either been fine-tuned to ultimately have the O<sub>2</sub> column  
319 density match with that estimated by Hall et al. (1998) (Leblanc et al., 2017),

320 or estimated by combining laboratory data on photolysis and radiolysis rates  
321 with ion fluxes measured by the EPD instrument during the close Galileo  
322 flybys (e.g. Shematovich (2016); Marconi (2007)), or again calculated by  
323 dynamically simulating the impact of Jovian ions on the moon's surface and  
324 making assumptions regarding the sputtering yields (Plainaki et al., 2015).  
325 However, the yield values have not been confirmed by direct measurements.  
326 Different models implemented ejection rates which differ by more than one  
327 order of magnitude (e.g. Plainaki et al. (2015) and Leblanc et al. (2017)). The  
328 source of uncertainty comes primarily from the sputtering yield associated  
329 with the ion impact, which depends on several parameters, many of which  
330 related to the detailed surface structure, which are not easy to estimate and  
331 replicate with laboratory experiments.

332 The discrepancy with observations found by the ionospheric model hints  
333 that the ejection rates used in the model of Leblanc et al. (2017), which is  
334 a driver of the ionospheric model, could be underestimated. Teolis et al.  
335 (2009) showed that the ejection rate of  $O_2$  is not directly correlated to the  
336 incoming flux of energetic ions impacting the surface; they showed that  $O_2$   
337 is formed within the surface and accumulates before being released into the  
338 atmosphere, i.e., it is not sputtered immediately. As a consequence, the  
339 ejection rate of this species cannot either be easily quantified from simulations  
340 of plasma impacting Ganymede's surface. Estimates usually assume that the  
341 production of  $H_2/O_2$  is a constant fraction of the  $H_2O$  ejected (like assumed  
342 by Leblanc et al. (2017)). However, Teolis et al. (2017) showed that, in fact,  
343 the relative yield is highly dependent on the energy of the impacting ion.  
344 Bearing in mind that the  $O_2$  ejection rate is poorly constrained, we have

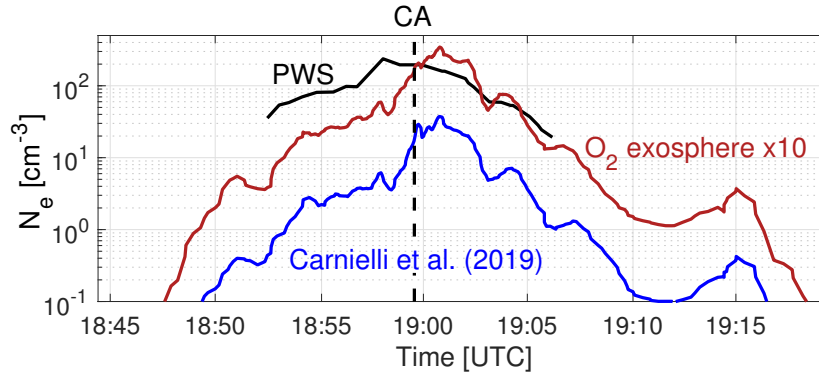


Figure 4: Electron number density along the G2 flyby as recorded by: the PWS instrument (black curve), an ionospheric simulation with the input exosphere from the model of Leblanc et al. (2017) (blue curve), and an ionospheric simulation run with the same exosphere boosted by a factor of 10 (red curve).

345 assessed how the discrepancy in electron number density along the G2 flyby  
 346 varies in relation to a change of the  $O_2$  distribution.

347 To increase the ion production rate we multiplied by 10 the  $O_2$  distri-  
 348 bution derived by Leblanc et al. (2017). This corresponds to assuming that  
 349 the dynamics of molecules is exactly like the one simulated by Leblanc et al.  
 350 (2017), but the ejection rate is increased by a factor of 10. Due to the lack of  
 351 constraints for the ejection rate and the poor constraints on the column den-  
 352 sity, we argue that a boost by a factor of 10 is possible. This would bring the  
 353 mean column density of  $O_2$ , the only “observational constraint”, to  $2.44 \times 10^{15}$   
 354  $\text{cm}^{-2}$ , which is just a factor of 2 higher than the upper limit estimated by  
 355 Hall et al. (1998).

356 The electron density along the G2 flyby that results from an ionospheric  
 357 simulation using this boosted configuration is plotted in red in Figure 4, while  
 358 the blue curve shows the one obtained from an ionospheric simulation using



359 the original exospheric configuration of Leblanc et al. (2017). Note that the  
360 red curve almost corresponds to the blue curve shifted upward by one order  
361 of magnitude. Even with the  $O_2$  density increased by a factor of 10, collisions  
362 still leave almost unaffected the ionospheric configuration along the G2 flyby,  
363 and only near closest approach some differences are noticed. For the boosted  
364 exosphere case, there is a good match with PWS data in the outbound leg  
365 of the flyby, but there is still a discrepancy in the inbound leg, with the  
366 simulated density still lower compared to the measured values. This indicates  
367 that if the  $O_2$  exosphere is considered as the only cause for the discrepancy,  
368 then the density of neutral species must be further increased in the region  
369 where test particles crossing the spacecraft trajectory in the inbound leg  
370 are produced.  $O_2^+$  test particles crossing the Galileo G2 trajectory in the  
371 inbound leg are produced in the anti-Jovian hemisphere, while those crossing  
372 in the outbound leg are primarily produced in the Jovian-facing hemisphere  
373 (not shown). In order to have the electron number density match also in  
374 the inbound leg of the flyby, the  $O_2$  distribution would have to be locally  
375 increased by an additional factor of 4 in the anti-Jovian hemisphere, at least  
376 in the region of open magnetic field lines. In the exospheric model of Leblanc  
377 et al. (2017), a longitudinal asymmetry features in the equatorial region due  
378 to the accumulation of  $O_2$  in the afternoon side due to Ganymede's rotation,  
379 but such an asymmetry amounts to less than a factor of 2, and is confined  
380 to the low latitudes. Elsewhere,  $O_2$  distributes homogeneously as it does not  
381 stick to the surface. Being unable to find a physical justification to explain a  
382 factor of 4 difference in the  $O_2$  number density in the polar regions, we have  
383 concluded that the  $O_2$  distribution alone cannot justify the discrepancy.

384 It could be argued that  $O_2$  might not be the only underestimated neu-  
385 tral species in the model of Leblanc et al. (2017). Indeed, the exospheric  
386 model could not reproduce the Ly- $\alpha$  emission lines observed by the Galileo  
387 UV spectrometer, which suggests that the H exosphere simulated might be  
388 underestimated. However, we have checked that boosting the density of all  
389 neutral species by 10 yields the same result as boosting only the  $O_2$  distri-  
390 bution for the purpose of matching the electron number density along the  
391 G2 flyby because the latter species largely dominates the plasma composi-  
392 tion (see Figure C.13 in Carnielli et al. (2019)). Moreover, the other neutral  
393 species do not accumulate in the surface like  $O_2$ , hence their ejection rate is  
394 more constrained than that of  $O_2$ .

#### 395 **4. Electron-impact ionization frequency revisited**

396 If the exosphere is not responsible alone for the discrepancy between the  
397 observed and modeled electron densities along the G2 trajectory, the only  
398 other option left is the ionization frequency. In the ionospheric model, the  
399 neutral exosphere is ionized by solar EUV radiation and Jovian magneto-  
400 spheric electrons. On the one hand, the photo-ionization process is derived  
401 from the solar flux, which is known with a good level of confidence. On the  
402 other hand, the electron-impact ionization frequency, which is an order of  
403 magnitude larger than the photo-ionization frequency (Carnielli et al., 2019),  
404 is less certain and potentially too strong assumptions have been made in the  
405 ionospheric model. Here, we review in more detail the way the electron-  
406 impact ionization frequency was calculated (Section 4.1). Then, we present  
407 results of simulations that implemented different electron-impact ionization

408 frequencies in different regions (Section 4.2), showing how this can signifi-  
409 cantly improve the comparison with observations.

#### 410 *4.1. Observations of energetic electrons*

411 The results presented thus far have been obtained from simulations in  
412 which the ionization frequency from electron-impact was calculated using the  
413 electron distribution outside Ganymede’s magnetosphere and set constant ev-  
414 erywhere outside the region of closed magnetic field lines (see Section 3.1.2  
415 in Carnielli et al., 2019). Figure 5 (top) shows the data from Scudder et al.  
416 (1981) we used to obtain the electron intensity along the G2 flyby in the  
417 energy range 12–5000 eV. The blue and yellow curves indicate the electron  
418 distribution functions recorded, respectively, by Voyager 1 and 2 in 1981  
419 during plasma sheet crossings at two different locations inside Jupiter’s mag-  
420 netosphere: one at  $12.87 R_J$  (blue) and the other at  $18.4 R_J$  (yellow). The  
421 green curve shows the profile interpolated at Ganymede’s orbital distance,  
422 at  $15.4 R_J$ . The interpolation was done linearly as an approximation. To  
423 interpolate the distribution at energies below 20 eV, the yellow curve was  
424 logarithmically extrapolated down to 12 eV.

425 The bottom panel of Figure 5 shows the electron intensity as a function  
426 of energy. The blue and red curves show measurements made during the  
427 G2 flyby, for which there is a good match in the overlapping energy range.  
428 The profile obtained from the conversion of the green curve on the top panel  
429 is shown by the curve of the same color in the bottom panel. For energies  
430 between 600 eV and 5000 eV, the slope of the green and blue profiles match  
431 well. The magnitude, however, is off by a factor of 2.8. This can be due to a  
432 multitude of reasons, including the fact that the measurements by Voyager

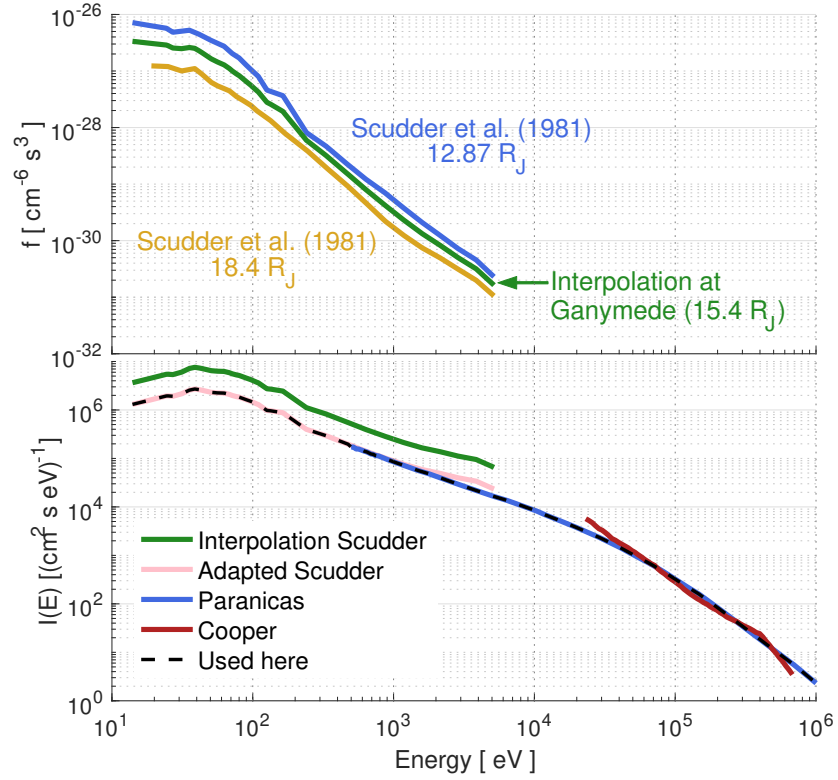


Figure 5: Top: Electron distribution function extracted from Scudder et al. (1981) (blue and yellow curves) at two distances from Jupiter in the magnetosphere and interpolated at Ganymede’s mean orbital distance (gray curve). Bottom: Electron differential flux as a function of energy, outside the Jovian plasma sheet near Ganymede. Isotropy was assumed. The gray curve shows the flux computed from the distribution function in Scudder et al. (1981) adapted to Ganymede’s orbital distance, the green curve shows the same but scaled to fit the blue curve in the shared energy range, the blue curve shows the flux presented in Paranicas et al. (1999), the red curve shows the flux presented in Cooper et al. (2001) and the dashed-black curve shows the combined flux adopted in our simulations.

433 1 and 2 were made when the spacecraft was inside the plasma sheet, while  
434 during the G2 flyby Galileo was above. In addition, the measurements of  
435 Voyager and Galileo were made at different epochs and positions, so it is  
436 very likely that the plasma conditions were not exactly the same between the  
437 two eras. As a consequence, the green profile was scaled down by a factor of  
438 2.8 (pink curve) in order to fit the Galileo measurements. The re-scaling of  
439 the data is justifiable in the energy range where data is available from both  
440 sets of measurements. However, for energies below approximately 500 eV the  
441 scaling factor might not be necessarily correct across the whole energy range.  
442 Because the highest ionization cross-sections for electron impact are found  
443 near 100 eV, the calculated ionization frequency could be slightly different  
444 from what has been derived in combining these datasets together.

445 In the ionospheric model we have assumed a constant electron-impact ion-  
446 ization frequency over the region of open magnetic field lines at Ganymede  
447 because there is no usable data available for the electron phase-space distribu-  
448 tion inside Ganymede's magnetosphere. Making such an assumption means  
449 that the effect of Ganymede's magnetosphere on the energetic electron pop-  
450 ulation is ignored. Williams et al. (1998) presented count rates for the very  
451 energetic electrons ( $>15$  keV) obtained by the PLS instrument along different  
452 flybys, including G2 (see Figure 1 in Williams et al., 1998). Although this  
453 dataset cannot be used directly to calculate the flux, it shows an asymmetry  
454 in the electron count rate between the inbound and outbound legs of the G2  
455 flyby, which is not considered in the ionospheric model. It is true that the  
456 latter is more concerned with electrons in the energy range near 100 eV, but  
457 it is possible that such an asymmetry could feature at lower energies as well.

458 This asymmetry arises because the spacecraft travels through two different  
459 regions of Ganymede’s magnetosphere. Before closest approach, it crossed a  
460 region with higher currents near the boundary between open and closed mag-  
461 netic field lines. After closest approach, it traveled for a relatively long time  
462 (23 minutes) inside the northern Alfvén wing, where the plasma flow is more  
463 laminar (see Figure 7 in Carnielli et al. (2019)). The difference in the plasma  
464 behavior between these two regions is clearly visible in the energy spectra (cf.  
465 Figure 8b in Carnielli et al., 2019). The profile in Figure 1 of Williams et al.  
466 (1998) shows that before closest approach the instrument recorded a higher  
467 count rate. If that is the case for electrons with lower energies, it would ex-  
468 plain the different slopes in the electron density profile recorded by the PWS  
469 instrument, which features a shallower slope in the inbound leg than in the  
470 outbound leg (see Figure 4). Hence, the ionization frequency could in fact be  
471 higher in the inbound leg of the G2 flyby. Moreover, the MHD model of Jia  
472 et al. (2008) found stronger currents in the anti-Jovian hemisphere compared  
473 to the Jovian-facing hemisphere for the G2 flyby conditions. Therefore, it is  
474 reasonable to argue that the actual ionization frequency could be different  
475 from what was originally assumed in our model and that the hemispheric  
476 asymmetry is indeed present.

#### 477 *4.2. Asymmetric electron-impact ionization frequency with boosted exosphere*

478 We have found that in order to obtain a good agreement in the inbound  
479 part of the flyby, the O<sub>2</sub> distribution needs to be boosted by a factor of 10 and  
480 the electron-impact ionization frequency needs to be increased by a factor of 4  
481 in the open magnetic field lines region around the subsolar longitude. This is  
482 plotted as the pink-shaded areas in Figure 6. The midday longitude is shown

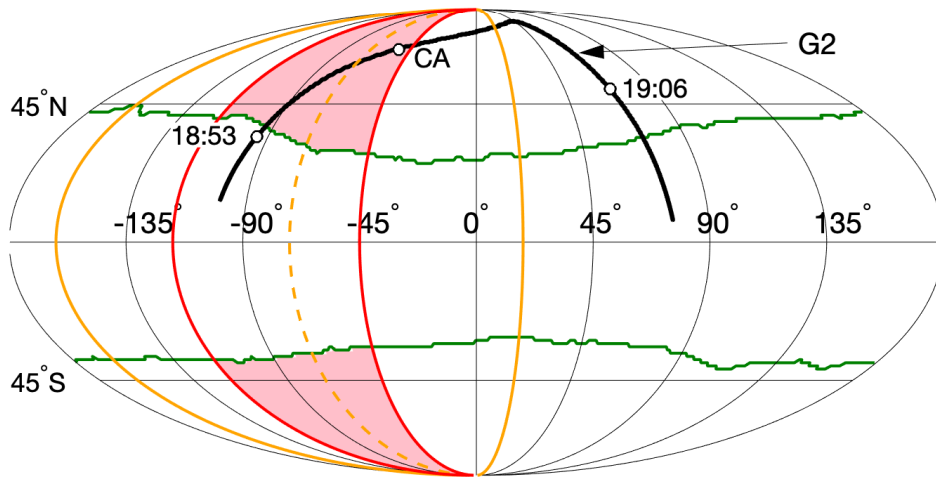


Figure 6: Mollweide projection of the G2 flyby trajectory (black line). In the longitudinal direction,  $0^\circ$  corresponds to the bisector of the leading hemisphere and  $90^\circ$  is towards Jupiter. The solid-orange line delimits the illuminated hemisphere and the dashed-orange line indicates the midday longitude. The pink-shaded areas, delimited by the red lines (at  $-117^\circ$  and  $-45^\circ$ ), identify the region of open magnetic field lines where the electron-impact ionization frequency was increased. The green lines show the surface boundary between open and closed magnetic field lines.

483 by the dashed-orange line, while the illuminated hemisphere is delimited by  
484 the solid-orange line. Figure 6 shows also the G2 flyby trajectory and the  
485 locations from/to which the electron number density was reported in Eviatar  
486 et al. (2001b) (18:53 UTC and 19:06 UTC). ‘CA’ indicates the location of  
487 closest approach. In the simulation, test particles crossing the G2 trajectory  
488 in the inbound leg are produced primarily near the spacecraft location (not  
489 shown), which almost coincides with the pink-shaded area in the northern  
490 hemisphere. The longitude range delimiting the pink regions, spanning from  
491  $-117^\circ$  to  $-45^\circ$ , is the one that was found leading to the best agreement with  
492 observations.

493 The electron number density (corresponding to the sum of all ion number  
494 densities) profile obtained by running the ionospheric model with this con-  
495 figuration is plotted in blue in Figure 7 (top panel). The fit with data (black  
496 curve) is very good over the inbound leg and the second half of the outbound  
497 leg, though the number density is overestimated by about a factor of 2–3  
498 near closest approach. The middle and bottom panels of Figure 7 show,  
499 respectively, the measured and modeled ion energy spectrogram, the latter  
500 implementing the suitably boosted exosphere. Compared to the spectrogram  
501 in Figure 8 of Carnielli et al. (2019), the shape of the energy distribution is  
502 unchanged, and remains in agreement with observations. However, the ion  
503 intensity is increased by the exospheric and electron-impact frequency boost,  
504 and now matches the observed intensity (panel b).

505 Considering the approach applied to evaluate the ionization frequency  
506 from electron impact with the associated uncertainties, the factor of 4 in-  
507 crease in the electron-impact ionization frequency does not seem unrealistic,



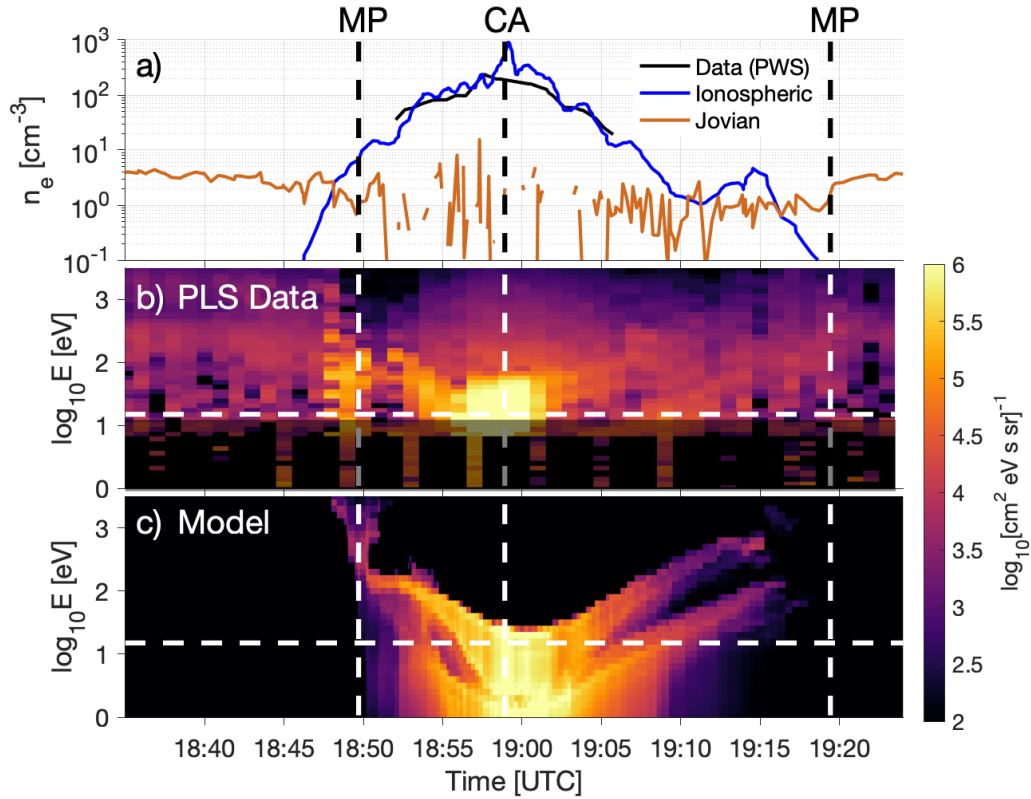


Figure 7: Top: Electron number density along the G2 flyby as a function of time as recorded by: the PWS instrument (black) and the ionospheric model (blue). The light brown profile shows the background Jovian ion density. Middle: Energy spectrogram as recorded by the PLS instrument. Bottom: Energy spectrogram as recorded by the ionospheric model. The white, dashed vertical lines indicate the times of magnetopause crossing (MP) and of closest approach (CA). The dashed, white horizontal lines in the middle and bottom panels show the upper energy limit below which the PLS dataset processing technique is considered as unreliable (see Carnielli et al. (2019) for more details). The simulation is driven by  $n_{O_2} \times 10$  (compared to Leblanc et al., 2017) and an asymmetric electron-impact ionization frequency.

508 unlike the way in which the exosphere would have to be boosted if exo-  
509 spheric densities were the only source of uncertainty. Electron-impact ion-  
510 ization cross-sections are sensitive to the electron energy below 100 eV, and  
511 inside Ganymede’s magnetosphere the electron energy distribution is affected  
512 by local processes, such as wave-particle interactions (Gurnett et al., 1996).  
513 Hence, it appears realistic to assume that the electron flux might be higher  
514 in correspondence to the strong currents at the Alfvén wings’ boundaries and  
515 that the electron-impact ionization frequency could be boosted by as much  
516 as a factor of 4.

517 Although we find a good match in the electron number density along  
518 the G2 trajectory when boosting exospheric densities by a factor of 10 and  
519 the electron-impact ionization frequency by a factor of 4 in the anti-Jovian  
520 hemisphere, we acknowledge that this may not be the unique solution.

## 521 **5. Conclusions**

522 To date, Ganymede’s neutral and plasma environments remain poorly  
523 constrained due to the lack of data. While waiting for new plasma, particle,  
524 and neutral data to come with the ESA JUICE mission, modeling efforts can  
525 be made to try improving our understanding of these physical environments  
526 and get the scientific community prepared for the mission. In this context,  
527 our ionospheric model is relevant to simulating the ion energy distribution  
528 and moments to be measured by PEP and RPWI instruments on board the  
529 JUICE spacecraft, and the modeling of hot O<sub>2</sub> presented in Appendix A is  
530 relevant to PEP as this population will be probed by its neutral channel.

531 Building from the original ionospheric model developed by Carnielli et

532 al. (2019), we have investigated the neutral and plasma environments with  
533 the aim of finding a suitable configuration for the neutral exosphere and  
534 ionosphere in order to solve the discrepancy in the electron number density  
535 along the G2 flyby found by Carnielli et al. (2019). First, we have im-  
536 proved the ionospheric model by developing a collision scheme, simulating  
537 the energetic component of the input O<sub>2</sub> exosphere (absent in the exosphere  
538 modeled by Leblanc et al. (2017)) and adding it to the original exospheric  
539 O<sub>2</sub> distribution. Charge-exchange collisions lead to an increased ionospheric  
540 density close to the surface, but they cannot provide an explanation for the  
541 discrepancy between the model and Galileo observations in terms of elec-  
542 tron number density. Hence, we have identified the neutral exosphere and  
543 the ionization frequency from electron-impact as the possible causes for this  
544 discrepancy. We have found that the O<sub>2</sub> exosphere should be denser than  
545 what has been published from observation-driven estimates (e.g., Hall et al.  
546 (1998), Feldman et al. (2000)) and those derived from previous exospheric  
547 models. More precisely, we find that the average O<sub>2</sub> column density should  
548 be  $\sim 2.5 \times 10^{15} \text{ cm}^{-2}$ , i.e., higher than the range of  $10^{14}$ – $10^{15} \text{ cm}^{-2}$  derived  
549 by Hall et al. (1998) and a factor of 10 higher compared to the value found  
550 by the model of Leblanc et al. (2017). The comparison with Broadfoot et al.  
551 (1981) is limited since they only provided an upper limit for the exospheric  
552 surface density ( $1.5 \times 10^9 \text{ cm}^{-3}$ ), and not for the column density. Consider-  
553 ing only this value and assuming the same scale height as in the model of  
554 Leblanc et al. (2017)), the required exospheric configuration is within the  
555 limit derived by Broadfoot et al. (1981). As for the electron-impact ioniza-  
556 tion frequency, the discrepancy with Galileo observations can be solved if

557 this parameter acts asymmetrically in the northern polar region with respect  
558 to the Jovian and anti-Jovian hemispheres, being about 4 times stronger in  
559 the latter (at least for the configuration of Ganymede during the G2 epoch).  
560 This asymmetry is supported by observations of the electron count rate by  
561 the EPD instrument (Williams et al., 1998). While there are uncertain-  
562 ties on these numbers, the key message is that only a boosted exosphere  
563 can realistically explain the underestimated electron density, and that the  
564 electron-impact ionization frequency likely acts asymmetrically between the  
565 Jovian and anti-Jovian hemispheres.

566 The next key step required to improve the quality of our study includes  
567 simulating the Jovian electron distribution inside Ganymede’s magnetosphere.  
568 Having the 3D distribution of Jovian electrons inside the magnetosphere  
569 would allow to have a more realistic map of the ionization process of the neu-  
570 tral exosphere, which would improve the ionospheric model. Furthermore,  
571 it would allow to estimate more accurately the O<sub>2</sub> column density from the  
572 observed FUV emissions, since thus far too strong assumptions have been  
573 made for the exciting electrons producing these emissions.

## 574 **6. Acknowledgments**

575 Work at Imperial College London was supported by STFC of UK through  
576 a postgraduate studentship under grant ST/N000692/1. FL and RM ac-  
577 knowledge the support by the ANR HELIOSARES (ANR-09-BLAN-0223),  
578 ANR MARMITE-CNRS (ANR-13-BS05-0012-02) and by the “Système So-  
579 laire” program of the French Space Agency CNES. XJ acknowledges support  
580 by NASA’s Solar System Workings program through grant NNX15AH28G.

581 Authors also warmly acknowledge the support of the IPSL data centre CI-  
582 CLAD for providing access to their computing resources.

## Appendix A. Simulation of energetic neutrals

Leblanc et al. (2017) did not include any form of energetic neutrals in their model. These can be generated from the high energy tail of the distribution with which particles are ejected from the surface or from charge-exchange with ions, which can be from Ganymede’s ionosphere or from Jupiter’s magnetosphere. As the distribution of ionospheric ions was not available, Leblanc et al. (2017) neglected the charge-exchange process, obtaining an exosphere dominated by  $O_2$  confined close to the surface. With the ionospheric model we have developed, it is possible to simulate this process and get a more realistic  $O_2$  distribution at high altitudes.

The first step required to calculate the distribution of energetic neutrals is to determine their production rate as a function of position. This can be calculated while running the test particle code for the ion species selected for the charge-exchange process. We have considered Reactions (1) and (2), driven by ionospheric  $O_2^+$  and ionospheric and Jovian  $O^+$ , which become, respectively, fast  $O_2$  and fast  $O$  by reacting with  $O_2$ . At each iteration, a fraction of the test particle is neutralized by charge-exchange. The amount produced is recorded at each cell of the exospheric grid, together with the velocity and its spread. At the end of the simulation, 3D maps are generated for the production rate ( $cm^{-3} s^{-1}$ ), average velocity, and average square velocity components of the energetic neutral species. Subsequently, a new simulation is run where the injected test particles are energetic neutrals in-

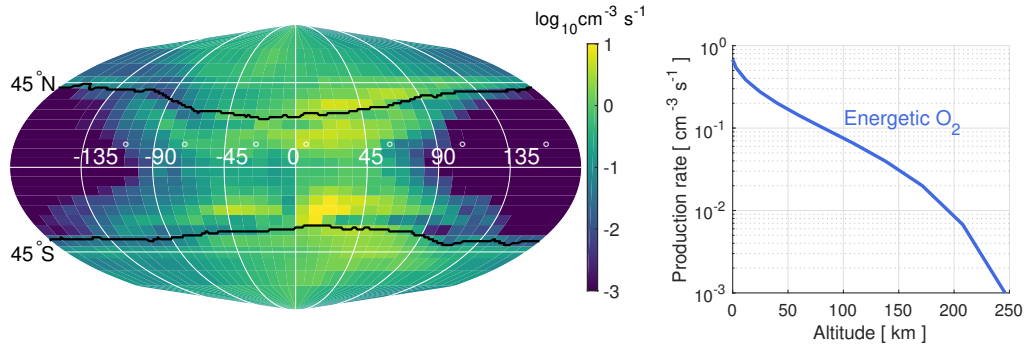


Figure A.8: Left panel: Map of  $O_2$  production rate from charge-exchange with  $O_2^+$  at the surface. In the longitudinal direction,  $0^\circ$  and  $90^\circ$  correspond to the bisectors of, respectively, the leading and Jovian-facing hemispheres. The black curves show the OCFB lines obtained from the MHD model of Jia et al. (2009). The color scale is logarithmic. Right panel: Average (over latitude and longitude) production rate of  $O_2$  from charge-exchange with  $O_2^+$  as a function of altitude.

stead of ionospheric ions. This is performed by loading the production map of energetic neutrals instead of the neutral exosphere. For such a simulation, in which test particles are electrically neutral, the only force felt is gravity, so the code behaves like an exospheric one. Like for the ionospheric simulation, test particles are followed either until they impact the moon's surface, or until they leave the simulation volume. Finally, 3D maps for the distribution of energetic neutral species are generated like for ionospheric ions.

According to our simulations, the most important charge-exchange reaction, in terms of occurrence, is that between  $O_2$  and  $O_2^+$ , hence only results for this particular interaction are described here. However, the updated exospheric maps that have been subsequently used in our ionospheric model were produced considering also the interaction of  $O_2$  with ionospheric and Jovian  $O^+$ . Figure A.8 shows the production rate of energetic  $O_2$  produced

from charge-exchange with  $\text{O}_2^+$ . The left panel shows the distribution of the production rate over the surface, while the right panel shows the average value (over latitude and longitude) as a function of altitude, which follows closely the  $\text{O}_2$  variation in the model of Leblanc et al. (2017) (not shown). Over the altitude range in which collisions occur (within  $0.1 R_G \equiv 263$  km) the latitude-longitude distribution does not vary significantly in altitude, hence the two panels in Figure A.8 give a complete account of the energetic hot  $\text{O}_2$  production map. The production rate at the surface peaks at about  $10 \text{ cm}^{-3}\text{s}^{-1}$  and is found at low latitudes in the afternoon sector (between  $0^\circ$  and  $90^\circ$ , see left panel). This region corresponds to the maximum in exospheric  $\text{O}_2$  density in the model of Leblanc et al. (2017), so collisions are more frequent. Although the  $\text{O}_2$  exosphere is spread more or less constantly in the model of Leblanc et al. (2017), the left panel of Figure A.8 shows a clear asymmetry between the leading and trailing hemisphere in terms of production rate. This is because for the G2 flyby conditions ionospheric ions do not populate the trailing hemisphere at low altitudes (Carnielli et al., 2019), which reflects also in the production map of hot  $\text{O}_2$ . According to the ionospheric simulations,  $\text{O}_2^+$  is produced mainly in the polar regions, and drifts toward the leading hemisphere at low latitudes, explaining the increased collision frequency, or equivalently the production rate of hot  $\text{O}_2$  in this region.

Figure A.9 shows 2D maps of the number density of energetic  $\text{O}_2$  in the XZ, YZ and XY planes (see figure caption for a description of the coordinate system). The maps have some similarities compared to that of  $\text{O}_2^+$  (cf. Figure A.12 in Carnielli et al., 2019): the regions with higher number density

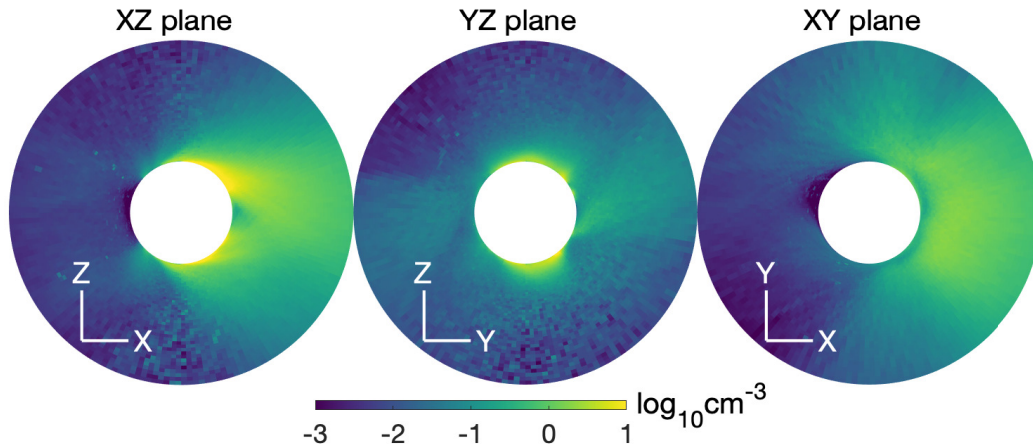


Figure A.9: Number density (in logarithmic color scale) of energetic  $O_2$  resulting from charge-exchange with ionospheric  $O_2^+$  in the XZ (left), YZ (middle) and XY (right) planes. X points in the direction of corotation of the Jovian plasma, Y points towards Jupiter and Z completes the right-handed coordinate system.

are the polar regions and the equatorial region in the leading hemisphere. Due to their neutrality,  $O_2$  test particles are not tied to magnetic field lines and so do not mirror in the equatorial region. As a consequence, the rounded features seen in the  $O_2^+$  density maps that reproduce the magnetic field lines at low latitudes are not present. However, ‘jet-like structures’ appear in this region. These form from energetic ions mirroring in the closed-field lines region. They get neutralized by charge-exchange and continue their journey almost in a straight line due to their high velocity.

The green profile in Figure A.10 shows the average altitude distribution obtained for hot  $O_2$ . This is how the  $O_2$  distribution would extend if energetic neutrals were included in the model of Leblanc et al. (2017), for which the average altitude profile is plotted in blue. Above 250 km, the solid-blue curve decays in a physically unrealistic fashion. This problem is related to a lack



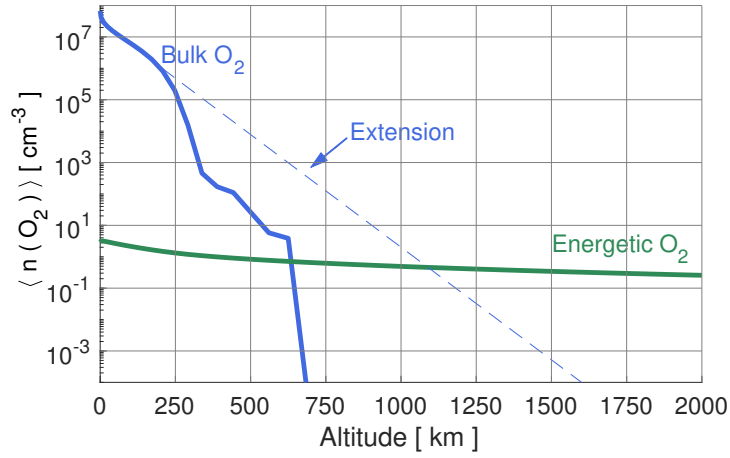


Figure A.10: Average number density as a function of altitude of the  $O_2$  (solid-blue line) population from the exospheric model of Leblanc et al. (2017) and the energetic  $O_2$  population produced through charge-exchange as simulated with the test particle code (green line). The dashed-blue line shows the extended profile of the bulk  $O_2$  population in an ideal simulation scenario (i.e., not limited by particle statistics).

of statistics at high altitudes in the exospheric model, which are reached by neutrals in the energetic tail of the velocity distribution. Having a good statistic sampling for the energetic tail, without too many particles describing the core of the distribution, is numerically time consuming. The dashed-blue line is an extension of the blue profile and shows how the latter would theoretically extend to higher altitudes in the absence of particle statistics issues.

After deriving the distribution of hot  $O_2$ , the green profile in Figure A.10 was added to the blue profile, and the ionospheric model has been run with this new updated exosphere. Despite yielding an improvement to the model, the total production rates of  $O_2^+$  and  $O^+$  ions deriving from ionization of  $O_2$  change negligibly since the neutral density at high altitudes is still 7 orders

of magnitude lower compared to that close to the surface, hence the effects on plasma moments are negligible as well.

The results of our calculations regarding the altitude distribution of energetic  $O_2$  can be compared to some extent with Marconi (2007), who also simulated charge-exchange collisions between  $O_2$  and  $O_2^+$ . However, Marconi (2007) assumed an  $O_2^+$  density considerably higher than that derived by our ionospheric model. In particular, Marconi (2007) assumed an exponentially decreasing density varying from  $2000 \text{ cm}^{-3}$  at the surface to  $70 \text{ cm}^{-3}$  at  $0.1 R_G$ , which is at all altitudes about two orders of magnitude higher than in our model. In addition, the model of Marconi (2007) ejected neutral particles with a different energy distribution compared to Leblanc et al. (2017), which contains an energetic tail. These particles also populate the higher altitudes. As a result, Marconi (2007) found a density for the energetic  $O_2$  population which is about 3 orders of magnitude higher compared to the profile shown in Figure A.10.

## References

- Banks, P., 1966. Collision frequencies and energy transfer. Ions. *Planetary Space Science* 14, 1105–1122. URL: <http://adsabs.harvard.edu/abs/1966P%26SS...14.1105B>, doi:10.1016/0032-0633(66)90025-0.
- Barth, C.A., Hord, C.W., Stewart, A.I.F., Pryor, W.R., Simmons, K.E., McClintock, W.E., Ajello, J.M., Naviaux, K.L., Aiello, J.J., 1997. Galileo ultraviolet spectrometer observations of atomic hydrogen in the atmosphere at Ganymede. *Geophysical Research Letters* 24, 2147. URL:

<http://adsabs.harvard.edu/abs/1997GeoRL..24.2147B>, doi:10.1029/97GL01927.

Broadfoot, A.L., Sandel, B.R., Shemansky, D.E., McConnell, J.C., Smith, G.R., Holberg, J.B., Atreya, S.K., Donahue, T.M., Strobel, D.F., Bertaux, J.L., 1981. Overview of the Voyager ultraviolet spectrometry results through Jupiter encounter. *Journal of Geophysical Research* 86, 8259–8284. URL: <http://adsabs.harvard.edu/abs/1981Sci...212..206B>, doi:10.1029/JA086iA10p08259.

Carlson, R.W., Bhattacharyya, J.C., Smith, B.A., Johnson, T.V., Hidayat, B., Smith, S.A., Taylor, G.E., O’Leary, B., Brinkmann, R.T., 1973. An Atmosphere on Ganymede from Its Occultation of SAO 186800 on 7 June 1972. *Science* 182, 53–55. URL: <http://adsabs.harvard.edu/abs/1973Sci...182...53C>, doi:10.1126/science.182.4107.53.

Carnielli, G., Galand, M., Leblanc, F., Leclercq, L., Huybrighs, H.L.F., Jia, X., 2019. First 3D test particle model of Ganymede’s ionosphere. *Icarus* URL: <http://www.sciencedirect.com/science/article/pii/S0019103517307054>, doi:10.1016/j.icarus.2019.04.016.

Cessateur, G., Lilensten, J., Barthélémy, M., Dudok de Wit, T., Simon Wedlund, C., Gronoff, G., Ménager, H., Kretschmar, M., 2012. Photoabsorption in Ganymede’s atmosphere. *Icarus* 218, 308–319. URL: <http://adsabs.harvard.edu/abs/2012JSWSC...2A..16C>, doi:10.1016/j.icarus.2011.11.025.

- Chanteur, G.M., Dubinin, E., Modolo, R., Fraenz, M., 2009. Capture of solar wind alpha-particles by the Martian atmosphere. *Geophysical Research Letters* 36, L23105. URL: <https://ui.adsabs.harvard.edu/abs/2009GeoRL..3623105C>, doi:10.1029/2009GL040235.
- Collinson, G., Paterson, W.R., Bard, C., Dorelli, J., Glocer, A., Sarantos, M., Wilson, R., 2018. New Results From Galileo's First Flyby of Ganymede: Reconnection-Driven Flows at the Low-Latitude Magnetopause Boundary, Crossing the Cusp, and Icy Ionospheric Escape. *Geophysical Research Letters* 45, 3382–3392. URL: <https://ui.adsabs.harvard.edu/abs/2018GeoRL..45.3382C>, doi:10.1002/2017GL075487.
- Cooper, J.F., Johnson, R.E., Mauk, B.H., Garrett, H.B., Gehrels, N., 2001. Energetic Ion and Electron Irradiation of the Icy Galilean Satellites. *Icarus* 149, 133–159. URL: <http://adsabs.harvard.edu/abs/2001Icar..149.133C>, doi:10.1006/icar.2000.6498.
- Eviatar, A., Strobel, D.F., Wolven, B.C., Feldman, P.D., McGrath, M.A., Williams, D.J., 2001a. Excitation of the Ganymede Ultraviolet Aurora. *The Astrophysical Journal* 555, 1013–1019. URL: <http://adsabs.harvard.edu/abs/2001ApJ...555.1013E>, doi:10.1086/321510.
- Eviatar, A., Vasyliūnas, V.M., Gurnett, D.A., 2001b. The ionosphere of Ganymede. *Planetary and Space Science* 49, 327–336. URL: <http://adsabs.harvard.edu/abs/2001P%26SS...49..327E>, doi:10.1016/S0032-0633(00)00154-9.

- Feldman, P.D., McGrath, M.A., Strobel, D.F., Moos, H.W., Retherford, K.D., Wolven, B.C., 2000. HST/STIS Ultraviolet Imaging of Polar Aurora on Ganymede. *The Astrophysical Journal* 535, 1085–1090. URL: <http://adsabs.harvard.edu/abs/2000ApJ...535.1085F>, doi:10.1086/308889.
- Frank, L.A., Paterson, W.R., Ackerson, K.L., Bolton, S.J., 1997. Outflow of hydrogen ions from Ganymede. *Geophysical Research Letters* 24, 2151. URL: <http://adsabs.harvard.edu/abs/1997GeoRL...24.2151F>, doi:10.1029/97GL01744.
- Gurnett, D.A., Kurth, W.S., Roux, A., Bolton, S.J., Kennel, C.F., 1996. Evidence for a magnetosphere at Ganymede from plasma-wave observations by the Galileo spacecraft. *Nature* 384, 535–537. URL: <http://adsabs.harvard.edu/abs/1996Natur.384...535G>, doi:10.1038/384535a0.
- Hall, D.T., Feldman, P.D., McGrath, M.A., Strobel, D.F., 1998. The Far-Ultraviolet Oxygen Airglow of Europa and Ganymede. *The Astrophysical Journal* 499, 475–481. URL: <http://adsabs.harvard.edu/abs/1998ApJ...499..475H>, doi:10.1086/305604.
- Jia, X., Walker, R.J., Kivelson, M.G., Khurana, K.K., Linker, J.A., 2008. Three-dimensional MHD simulations of Ganymede's magnetosphere. *Journal of Geophysical Research (Space Physics)* 113, A06212. URL: <http://adsabs.harvard.edu/abs/2008JGRA...113.6212J>, doi:10.1029/2007JA012748.
- Jia, X., Walker, R.J., Kivelson, M.G., Khurana, K.K., Linker, J.A., 2009. Properties of Ganymede's magnetosphere inferred from improved

- three-dimensional MHD simulations. *Journal of Geophysical Research (Space Physics)* 114, A09209. URL: <http://adsabs.harvard.edu/abs/2009JGRA...114.9209J>, doi:10.1029/2009JA014375.
- Kanik, I., Noren, C., Makarov, O.P., Vattipalle, P., Ajello, J.M., Shemansky, D.E., 2003. Electron impact dissociative excitation of O<sub>2</sub>: 2. Absolute emission cross sections of the OI(130.4 nm) and OI(135.6 nm) lines. *Journal of Geophysical Research (Planets)* 108, 5126. URL: <https://ui.adsabs.harvard.edu/abs/2003JGRE...108.5126K>, doi:10.1029/2000JE001423.
- Kliore, A.J., 1998. Satellite Atmospheres and Magnetospheres. *Highlights of Astronomy* 11, 1065. URL: <https://www.cambridge.org/core/services/aop-cambridge-core/content/view/S1539299600019602>.
- Koutroumpa, D., Modolo, R., Chanteur, G., Chaufray, J.Y., Kharchenko, V., Lallement, R., 2012. Solar wind charge exchange X-ray emission from Mars. Model and data comparison. *Astronomy & Astrophysics* 545, A153. URL: <https://ui.adsabs.harvard.edu/abs/2012A%26A...545A.153K>, doi:10.1051/0004-6361/201219720.
- Leblanc, F., Oza, A.V., Leclercq, L., Schmidt, C., Cassidy, T., Modolo, R., Chaufray, J.Y., Johnson, R.E., 2017. On the orbital variability of Ganymede's atmosphere. *Icarus* 293, 185–198. URL: <http://adsabs.harvard.edu/abs/2017Icar...293..185L>, doi:10.1016/j.icarus.2017.04.025.
- Leclercq, L., Modolo, R., Leblanc, F., Hess, S., Mancini, M., 2016. 3D magnetospheric parallel hybrid multi-grid method applied to planet-plasma

- interactions. *Journal of Computational Physics* 309, 295–313. URL: <http://adsabs.harvard.edu/abs/2016JCoPh.309..295L>, doi:10.1016/j.jcp.2016.01.005.
- Lindsay, B.G., Stebbings, R.F., 2005. Charge transfer cross sections for energetic neutral atom data analysis. *Journal of Geophysical Research (Space Physics)* 110, A12213. URL: <http://adsabs.harvard.edu/abs/2005JGRA..11012213L>, doi:10.1029/2005JA011298.
- Marconi, M.L., 2007. A kinetic model of Ganymede’s atmosphere. *Icarus* 190, 155–174. URL: <http://adsabs.harvard.edu/abs/2007Icar..190..155M>, doi:10.1016/j.icarus.2007.02.016.
- McGrath, M.A., Jia, X., Retherford, K., Feldman, P.D., Strobel, D.F., Saur, J., 2013. Aurora on Ganymede. *Journal of Geophysical Research (Space Physics)* 118, 2043–2054. URL: <http://adsabs.harvard.edu/abs/2013JGRA..118.2043M>, doi:10.1002/jgra.50122.
- Modolo, R., Hess, S., Mancini, M., Leblanc, F., Chaufray, J.Y., Brain, D., Leclercq, L., Esteban-Hernández, R., Chanteur, G., Weill, P., González-Galindo, F., Forget, F., Yagi, M., Mazelle, C., 2016. Mars-solar wind interaction: LatHyS, an improved parallel 3-D multispecies hybrid model. *Journal of Geophysical Research (Space Physics)* 121, 6378–6399. URL: <https://ui.adsabs.harvard.edu/abs/2016JGRA..121.6378M>, doi:10.1002/2015JA022324.
- Molyneux, P.M., Nichols, J.D., Bannister, N.P., Bunce, E.J., Clarke, J.T., Cowley, S.W.H., Gérard, J.C., Grodent, D., Milan, S.E., Paty, C., 2018.

- Hubble Space Telescope Observations of Variations in Ganymede's Oxygen Atmosphere and Aurora. *Journal of Geophysical Research (Space Physics)* 123, 3777–3793. URL: <http://adsabs.harvard.edu/abs/2018JGRA..123.3777M>, doi:10.1029/2018JA025243.
- Neubauer, F.M., 1998. The sub-Alfvénic interaction of the Galilean satellites with the Jovian magnetosphere. *Journal of Geophysical Research* 103, 19843–19866. URL: <http://adsabs.harvard.edu/abs/1998JGR...10319843N>, doi:10.1029/97JE03370.
- Paranicas, C., Paterson, W.R., Cheng, A.F., Mauk, B.H., McEntire, R.W., Frank, L.A., Williams, D.J., 1999. Energetic particle observations near Ganymede. *Journal of Geophysical Research* 104, 17459–17470. URL: <http://adsabs.harvard.edu/abs/1999JGR...10417459P>, doi:10.1029/1999JA900199.
- Paty, C., Paterson, W., Winglee, R., 2008. Ion energization in Ganymede's magnetosphere: Using multifluid simulations to interpret ion energy spectrograms. *Journal of Geophysical Research (Space Physics)* 113, A06211. URL: <http://adsabs.harvard.edu/abs/2008JGRA..113.6211P>, doi:10.1029/2007JA012848.
- Plainaki, C., Milillo, A., Massetti, S., Mura, A., Jia, X., Orsini, S., Mangano, V., De Angelis, E., Rispoli, R., 2015. The H<sub>2</sub>O and O<sub>2</sub> exospheres of Ganymede: The result of a complex interaction between the jovian magnetospheric ions and the icy moon. *Icarus* 245, 306–319. URL: <http://adsabs.harvard.edu/abs/2015Icar..245..306P>, doi:10.1016/j.icarus.2014.09.018.



- Scudder, J.D., Sittler, E.C., Bridge, H.S., 1981. A survey of the plasma electron environment of Jupiter - A view from Voyager. *Journal of Geophysical Research* 86, 8157–8179. URL: <http://adsabs.harvard.edu/abs/1981JGR...86.8157S>, doi:10.1029/JA086iA10p08157.
- Shematovich, V.I., 2016. Neutral atmosphere near the icy surface of Jupiter's moon Ganymede. *Solar System Research* 50, 262–280. URL: <http://adsabs.harvard.edu/abs/2016SoSyR...50..262S>, doi:10.1134/S0038094616040067.
- Stebbing, R.F., Turner, B.R., Smith, A.C.H., 1963. Charge Transfer in Oxygen, Nitrogen, and Nitric Oxide. *Journal of Chemical and Physical Reference Data* 38, 2277–2279. URL: <http://adsabs.harvard.edu/abs/1963JChPh...38.2277S>, doi:10.1063/1.1733961.
- Teolis, B.D., Plainaki, C., Cassidy, T.A., Raut, U., 2017. Water Ice Radiolytic O<sub>2</sub>, H<sub>2</sub>, and H<sub>2</sub>O<sub>2</sub> Yields for Any Projectile Species, Energy, or Temperature: A Model for Icy Astrophysical Bodies. *Journal of Geophysical Research (Planets)* 122, 1996–2012. URL: <https://ui.adsabs.harvard.edu/abs/2017JGRE...122.1996T>, doi:10.1002/2017JE005285.
- Teolis, B.D., Shi, J., Baragiola, R.A., 2009. Formation, trapping, and ejection of radiolytic O<sub>2</sub> from ion-irradiated water ice studied by sputter depth profiling. *The Journal of Chemical Physics* 130, 134704–134704. URL: <http://adsabs.harvard.edu/abs/2009JChPh.130m4704T>, doi:10.1063/1.3091998.

- Turc, L., Leclercq, L., Leblanc, F., Modolo, R., Chaufray, J.Y., 2014. Modelling Ganymede's neutral environment: A 3D test-particle simulation. *Icarus* 229, 157–169. URL: <http://adsabs.harvard.edu/abs/2014Icar..229..157T>, doi:10.1016/j.icarus.2013.11.005.
- Vasyliūnas, V.M., Eviatar, A., 2000. Outflow of ions from Ganymede: A reinterpretation. *Geophysical Research Letters* 27, 1347–1349. URL: <http://adsabs.harvard.edu/abs/2000GeoRL..27.1347V>, doi:10.1029/2000GL003739.
- Williams, D.J., Mauk, B., McEntire, R.W., 1998. Properties of Ganymede's magnetosphere as revealed by energetic particle observations. *Geophysical Research Letters* 103, 17523–17534. URL: <http://adsabs.harvard.edu/abs/1998JGR...10317523W>, doi:10.1029/98JA01370.
- Zhou, H., Tóth, G., Jia, X., Chen, Y., Markidis, S., 2019. Embedded Kinetic Simulation of Ganymede's Magnetosphere: Improvements and Inferences. *Journal of Geophysical Research* 124. doi:10.1029/2019JA026643.